The International Journal of Advanced Manufacturing Technology (2022) 118:3487–3496
https://doi.org/10.1007/s00170-021-07402-x

APPLICATION

Calibration of five-axis motion platform based on monocular vision

Qiang Lu [1,2] · Haibo Zhou [1,2] · Zhiqiang Li [1,2] · Xia Ju [1,2] · Shuaixia Tan [3] · Ji'an Duan [1,2]

Received: 6 December 2020 / Accepted: 1 June 2021 / Published online: 14 October 2021

Abstract
In order to solve the problem of high measurement cost and complex operation of position-independent geometric errors (PIGEs) calibration on a five-axis motion platform, this paper first proposes a low-cost pose measurement method, based on monocular vision, which can accurately determine the pose in the environment, even with image shadow and noise. Next, an improved method, combining pose measurement and kinematic parameters identification, is proposed to calibrate a five-axis motion platform. The kinematic error model of the platform and the pose planning of automatic image acquisition are established, providing the pose data and motor position data, required for calibration. Combined with the kinematic loop method, the kinematic parameters of the five-axis motion platform are identified, while the geometric structure parameters are accurately calibrated. Before and after calibration, a circular trajectory of the target coordinate system (TCS) origin, relative to the camera coordinate system (CCS), is used to test the comprehensive accuracy evolution of the five-axis motion platform, by comparing the position and orientation errors of the theoretical circle trajectory to the actual one. The experimental data show that, before and after calibration, the average position error of the five-axis motion platform is reduced by 79.46%, while the average direction error is reduced by 86.53%. The experimental results clearly demonstrate that the proposed calibration method significantly improves the comprehensive motion accuracy of the five-axis motion platform, and they verify the practical value and effectiveness of the calibration scheme.

Keywords Monocular vision · Pose measurement · Kinematic parameters calibration · Five-axis motion platform

1 Introduction

Accuracy is one of the most important key performance indicators (KPIs) of the five-axis motion platform. A command is given to this mechanism with three translation axes and two rotation axes, to make it reach the designated pose. The ideal situation is where the actual pose of the five-axis motion platform identifies with the commanded pose. However, due to various reasons, the five-axis motion platform cannot reach the designated pose, which leads to the spatial geometric error. According to the motion characteristics of geometric errors, they are usually divided into position-dependent geometric errors (PDGEs) and position-independent geometric errors (PIGEs). PDGEs are mainly caused by manufacturing defects of mechanical parts, such as the straightness error of the guide rail [1], while PIGEs are mainly caused during the assembly of mechanical parts [2]. The error, caused by mechanical parameters deviation, accounts for 65–95% of the total system error, in the kinematics equation. The geometric structure parameters are used to represent the geometric relationship of motion axes. For the five-axis motion platform, in ideal state, the three linear axes are perpendicular to each other, and the two rotary axes are vertical and intersecting. However, the platform will be affected by processing errors, installation errors, and other factors. For the PIGEs caused by installation, there are squareness errors in linear axis and angular errors and position errors in rotary axis [3]. Due to the cumulative effect of these errors, the ideal geometric structure relationships are difficult to achieve. There is a certain deviation between the actual geometry parameters and the design parameters of the five-axis motion platform. This deviation leads to inaccurate control modeling of multi-axis motion platform, which reduces the derived absolute accuracy of the construction [4–6].

✉ Shuaixia Tan
65453639@qq.com

[1] College of Mechanical and Electrical Engineering, Central South University, Changsha 410000, Hunan, China

[2] State Key Laboratory of High Performance Complex Manufacturing, Central South University, Changsha 410000, Hunan, China

[3] Zhuzhou Times New Material Technology Co., Ltd., Zhuzhou 412007, Hunan, China

This paper mainly studies the measurement, identification, analysis, and compensation of PIGEs of a five-axis motion platform. The different measurement methods of five-axis motion platform geometric errors can be divided into direct and indirect methods [7, 8]. According to the direct measurement method, a device is used to directly measure the error term of the platform. For example, a laser interferometer is usually used to measure the linear positioning error of a translational axis. The measurement accuracy of laser interferometer can reach submicron accuracy, but its measurement process is complex and time-consuming. Based on the indirect measurement method, the mathematical model of the relation between the pose error of the end effector and geometric error elements is first established, while the geometric error parameters are identified by measuring the pose error of the end effector. Due to its high efficiency, indirect measurement has become a research hotspot, in recent years. Various measuring instruments have been designed and used to calibrate geometric errors efficiently, based on the indirect approach. Abbaszadeh-Mir et al. [9] used the ball-bar sensor to measure the position and orientation deviation of the tool center point of the five-axis motion platform, to achieve the identification of geometric errors. Fan [10] established the identifying model based on homogeneous transform matrix, while double ball bar (DBB) is adopted to test error motions of rotary axes. Jiang [11] established a five-axis machine tool model with homogeneous transformation matrices and proposed a testing scheme to diagnose the PIGEs of linear and rotary axes by using double ball bar. Zhang et al. [12] designed two DBB-measuring paths in different horizontal planes to evaluate simultaneously five errors including one axial error, two radial errors, and two tilt errors caused by the rotary table. Ibaraki et al. [13] proposed an efficient scheme to calibrate error motions of rotary axes on a five-axis machining center by using the R-test, while they present an algorithm to identify location errors and such position-dependent geometric errors. Hong et al. [14] proposed a scheme to separate squareness errors of linear axes by performing a set of R-test measurement to observe error motions of rotary axes. A touch trigger probe [15, 16] is also used to calibrate geometric errors. Mchichi [17] designed a measurement strategy for the indirect calibration of a five-axis machine tool using the Scale and Master Balls Artefact method.

In order to reduce the measurement cost and operation complexity of measuring instruments, many scholars use vision to derive a high-precision pose of five-axis motion platform and a robot to calibrate the geometric errors. Ibaraki [18] used a monocular camera to measure the two-dimensional position error of a five-axis motion platform, whereas Liu et al. [19] used a binocular camera to calibrate the parameters of PIGEs of the five-axis motion platform. Li et al. [20] proposed a 3D high temporal-spatial measurement method based on a monocular camera and realized the 3D detection of contouring errors of arbitrary paths. However, Li et al. only measured the contouring error and did not calibrate the geometric error of five-axis machine tool. In addition to the traditional vision measurement, Wang et al. [21] proposed a method of robot position error estimation, based on vision and neural network. Stepanova et al. [22] used RGB-D stereo camera to measure the pose of a robot end effector. Wang et al. [23] calibrated the parameters of body structure, hand eye structure, and camera system, using binocular vision, for a 6-DOF industrial robot.

In view of the high cost of current high-precision measurement equipment and the complexity of the calibration operation of five-axis motion platform, a low-cost pose measurement scheme, based on monocular vision, is proposed. The path planning is carried out, so as to automatically collect the platform end effector pose, while the pose error is calculated to realize the calibration of PIGEs of the five-axis motion platform. Before and after calibration, the five-axis motion platform moves on a circular trajectory of the target coordinate system (TCS) origin, relative to the camera coordinate system (CCS), through a five-axis linkage. The comprehensive accuracy variations of the five-axis motion platform, before and after calibration, are tested by comparing the position and orientation errors of the theoretical circle track to the respective ones of the actual circle track. The comparison of experimental results verifies the applicability and effectiveness of the calibration scheme.

The rest of this paper is organized as follows: Camera calibration model is expressed in Section 2. Section 3 portrays the method of target pose measurement and detection of pose measurement accuracy. Section 4 describes the calibration method of kinematic geometric parameters of five-axis motion platform using monocular vision. Experimental results and verifications of Calibration method for kinematic geometric parameters of five-axis motion platform are described in Section 5. The paper is concluded in Section 6.

2 Camera calibration model

The unit of a monocular camera can be roughly divided into three parts: lens, photosensitive chip, and processing circuit. When the light passes through the lens, the object to be photographed will produce an “image” on the photosensitive chip, which will be processed by the processing circuit, to derive a picture. As shown in Fig. 1, the monocular camera, used in this paper, is installed on the z-axis of the five-axis motion platform, while a high-precision checkerboard target (referred to as the target) is pasted on the c-axis. The spatial position of the camera is adjusted based on the motion along the X, Y and Z axes of the five-axis motion platform, while the spatial position of the target is determined by the motion along the A and C axes.

The imaging schematic diagram of the target, according to the ideal pinhole imaging model, is shown in Fig. 2, where

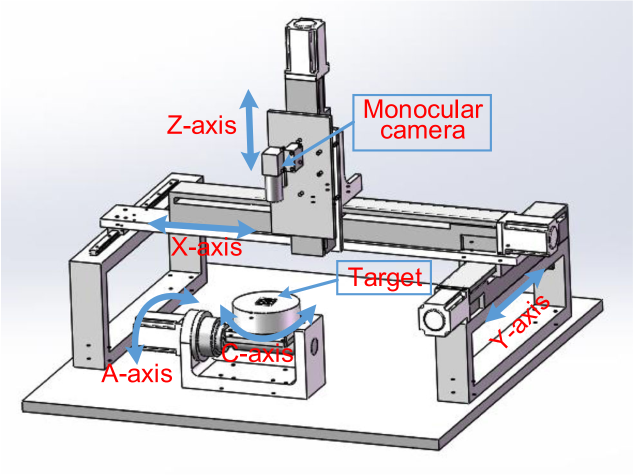

Fig. 1 Schematic structural diagram of five-axis motion platform

five coordinate systems are defined. The world coordinate system O_w-$X_wY_wZ_w$ is used as the datum coordinate system. In the camera CCS O_c-$X_cY_cZ_c$, the Z_c axis coincides with the optical axis of the camera. O_b-$X_bY_bZ_b$ is a three-dimensional rectangular coordinate system, referred to as the TCS, where the target is located on the X_bY_b plane. The image pixel coordinate system O_p-uv represents the coordinates of the object point on the imaging plane. The image physical coordinate system o-xy, with pixels as the unit, represents the position of o point in the imaging plane coordinate system.

As shown in Fig. 2, the coordinates of any corner M, on the calibration board, are X_b, Y_b, and Z_b in the TCS and X_c, Y_c, and Z_c in the CCS. According to the pinhole imaging principle, the intersection point, between the line segment MO_c and the imaging plane, is the image point m of the corner M. The coordinates of image point m, in the image pixel coordinate system, are u and v. The essence of calibration is to express the corner point coordinates in the form of pixel coordinates. Without considering lens distortion, the relationship [24, 25] between the coordinates (X_b, Y_b, Z_b) of corner point M, in the TCS, and the coordinates (u, v) of the corresponding image point m, in the image pixel coordinate system, is as follows:

$$Z_e\begin{bmatrix}u\\v\\1\end{bmatrix}=\begin{bmatrix}f_x&0&u_0&0\\0&f_y&v_0&0\\0&0&1&0\end{bmatrix}\begin{bmatrix}R&T\\0^T&1\end{bmatrix}\begin{bmatrix}X_b\\Y_b\\Z_b\\1\end{bmatrix}= \begin{bmatrix}p_1&p_2&p_3&p_4\\p_5&p_6&p_7&p_8\\p_9&p_{10}&p_{11}&p_{12}\end{bmatrix}\begin{bmatrix}X_b\\Y_b\\Z_b\\1\end{bmatrix}=M_1M_2\begin{bmatrix}X_b\\Y_b\\Z_b\\1\end{bmatrix} \tag{1}$$

where Z_b=0, u_0 and v_0 represent the pixel coordinates of the center o point on the imaging plane, and f_x and f_y denote the normalized focal length of the camera lens along the x-axis and y-axis. M_1 is the internal parameter matrix of the camera, which will remain constant, after the camera is installed and the focusing is concluded. M_2 is the external parameter matrix of the camera, which changes according to the pose of the TCS. R is the rotation matrix and T is the translation matrix of conversion from the TCS to the CCS.

Due to the manufacturing accuracy and installation technology of camera lens, the original image will be distorted, which will make the image point, as defined by the three-dimensional point projection, deviate from the ideal position. Therefore, the radial distortion coefficients K_1, K_2, and K_3 and tangential distortion coefficients P_1 and P_2 of the camera are introduced, to correct the image point position.

The internal parameters of the camera include camera internal parameter matrix and distortion coefficient vector. The camera internal parameters are calibrated based on the Zhang Zhengyou plane calibration method [26], so as to calculate more accurate target pose, according to the Perspective-N-Points (PNP) principle.

3 Target pose measurement and accuracy detection

PNP problem is a very important issue in computer vision. Using PNP principle to solve the target pose requires to accurately detect each corner on the target and to obtain the subpixel coordinates (u_i, v_i) of each corner point, in the image pixel coordinate system and the coordinates (X_{bi}, Y_{bi}, Z_{bi}) of each corner point in the TCS.

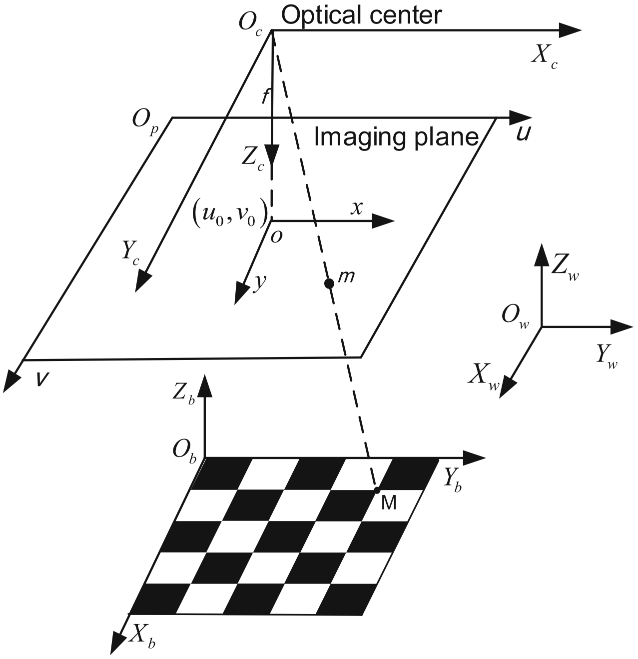

Fig. 2 Schematic diagram of checkerboard target imaging

3.1 Corner detection

For the planar checkerboard patterns used in this paper, the common corner imaging image is shown in Fig. 3. In order to detect the corners, 8 convolution kernels A_1, B_1, C_1, D_1, A_2, B_2, C_2, and D_2 are constructed to convolute with the collected target image. As shown in Fig. 4, in order to construct convolution kernels A_1, B_1, C_1, and D_1, the convolution kernel coordinate system $x_1o_1y_1$ is established. In Fig. 3, the position of corner a_1 is defined as the origin of coordinate system $x_1o_1y_1$, and the vertical boundary line and horizontal boundary lines of the a_1 point are X-axis and Y-axis, respectively. Defining r is the radius of convolution kernel, while the position coordinates of each element of the convolution kernel are x_i and y_i in Fig. 4.

The Gauss fuzzy convolution kernel equation is as follows:

$$G(x_i, y_i) = \frac{1}{2\pi r^2} \cdot e^{-\frac{(x_i{}^2+y_i{}^2)}{2r^2}} \tag{2}$$

According to Eq. (2), the weight value $G(x_i,y_i)$ of each convolution kernels element is obtained, while the elements in each quadrant of the convolution kernel coordinate system $x_1o_1y_1$ are normalized. Then the elements in quadrant *I* are proposed, while the rest of the elements in quadrant are assigned to 0, to obtain convolution kernel A_1. The elements in quadrant *III* are proposed, while the other elements in quadrant are assigned to 0, to obtain convolution kernel B_1. Also, the elements in quadrant *II* are proposed, while the rest elements in quadrant are assigned to 0, to obtain convolution kernel C_1. Finally, the elements in quadrant *IV* are proposed,

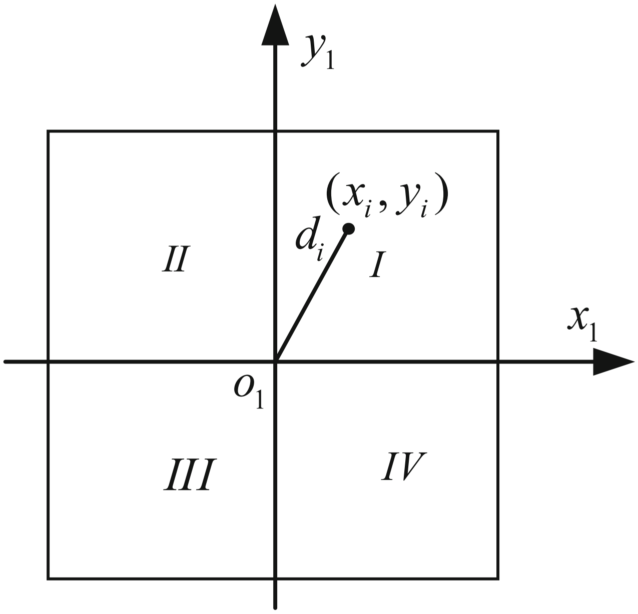

Fig. 4 The coordinates diagram of convolution kernel

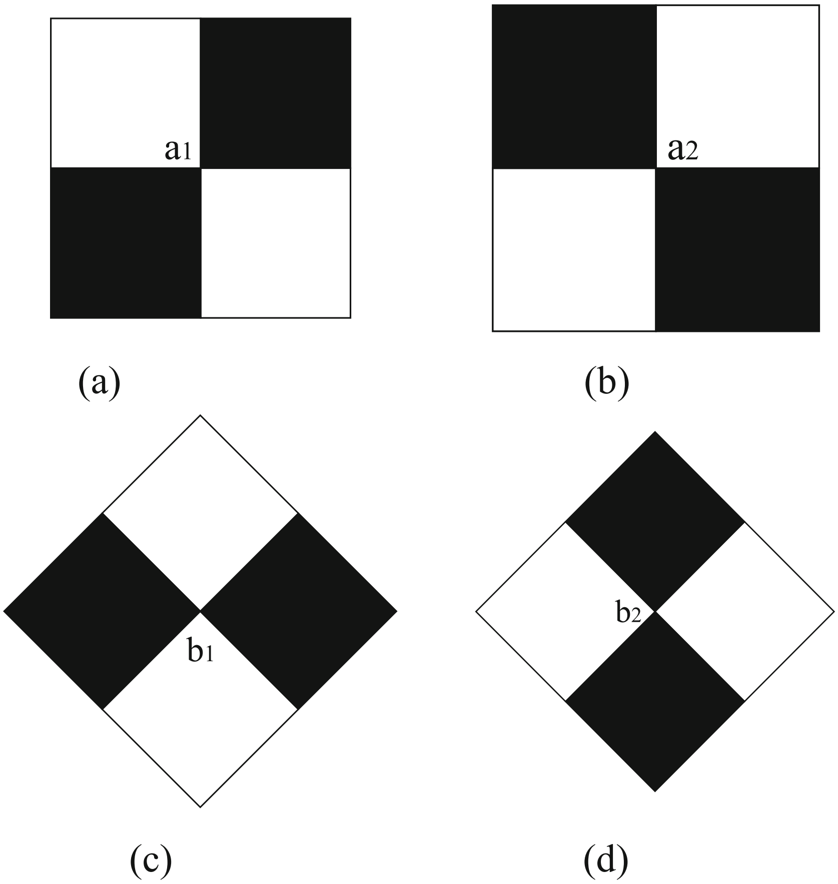

Fig. 3 The common corner imaging image: **a** corner imaging image a_1, **b** corner imaging image a_2, **c** corner imaging image b_1, and **d** corner imaging image b_2

while the other elements in quadrant are assigned to 0, to obtain convolution kernel D_1.

For the corner a_1 in Fig.3, the response of convolution kernels C_1 and D_1 is higher than that of convolution kernels A_1 and B_1, while the mean value of the responses of convolution kernels A_1, B_1, C_1, and D_1 is larger. Similarly, convolution kernels A_2, B_2, C_2, and D_2 can be constructed to detect corners b_1 and b_2 in Fig. 3.

The experimental results showed that the 8 convolution kernels can detect all corner imaging image of the chessboard calibration board, not only the four corner imaging images shown in Fig. 3. The total of 8 convolution kernels are used to convolute the pixels in the target image. The corner likelihood of each pixel in the image is calculated, forming the set **C**. A non-maximum suppression algorithm is used to filter and suppress the values in set **C**, to obtain the maximum points in the set **C**. These maximum points constitute the point set **Q** of the candidate points of the corner, thus obtaining the initial coordinates of the corner points [27].

The accuracy of the initial coordinates of the corners is not enough; thus, further optimization is needed. In this paper, the gray value gradient method [28] is used to determine the sub-pixel coordinates of corners. The basic principle is shown in Fig. 5. If the true position of the corner is point C, the points near point C can be divided into two categories: (a) the point on the edge, such as P in Fig. 5, and (b) the non-edge point, such as Q in Fig. 5. For an ideal corner, the gradient vector of point P is perpendicular to the edge, while the gradient value at point Q is zero. Therefore, all the points near the corner have the following characteristics:

$$\overrightarrow{\nabla C_i}\bullet\overrightarrow{CC_i}=0 \tag{3}$$

where C_i is any point in a region centered on C and $\overrightarrow{\nabla C_i}$ is the gradient vector at point C_i. This problem can be simplified into the following optimization problems:

$$c=\arg\min_{c_i}\sum_{c_i\in N_I(c)}\left(g_{c_i}^T(c_i-c)\right)^2 \tag{4}$$

The expression of the solution to the optimization problem is as follows:

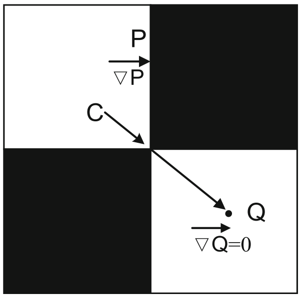

Fig. 5 Gradient diagram of corners

$$c=\left(\sum_{c_i\in N} g_{c_i}g_{c_i}^T\right)^{-1}\bullet\sum_{c_i\in N}\left(g_{c_i}g_{c_i}^T\right)c_i \tag{5}$$

In Eqs. (4) and (5), the small letters c and c_i represent the coordinates of point C and point C_i, respectively, g_{ci} represents the gradient vector at point C_i, while N represents the area near point c.

In order to use the detected corner pixel coordinates to solve the target pose, after detecting the sub-pixel coordinates of all corners, it is necessary to automatically sort the detected corner pixel coordinates. To this end, the energy method is used as a sorting algorithm, so as to derive the sub-pixel coordinates $(u_i\ ,v_i)$ of each corner in a specific order.

3.2 Solution of target pose

The inner corner of the target, as used in this paper, is in a 14 × 14 format, while the distance between adjacent corner points is 2mm. Each corner point is accordingly arranged on the target plane. The coordinates of each corner point are considered in the TCS, shown in Fig. 2. The sub-pixel coordinates $(u_i,\ v_i)$ of each corner are obtained, according to the method, presented in Section 2.1, while the PNP principle is used to solve the pose of the target. Considering Eq. (1), the *Zc* in the last line is eliminated, while the two constraints are obtained, as follows:

$$\begin{cases} u=\dfrac{p_1X_b+p_2Y_b+p_3Z_b+p_4}{p_9X_b+p_{10}Y_b+p_{11}Z_b+p_{12}} \\ v=\dfrac{p_5X_b+p_6Y_b+p_7Z_b+p_8}{p_9X_b+p_{10}Y_b+p_{11}Z_b+p_{12}} \end{cases} \tag{6}$$

In case there are N corners, let M_i=$(X_{bi},Y_{bi},Z_{bi},1)$, the obtained coordinates $(u_i\ ,v_i)$ and M_i are uniformly substituted into Eq. (6), and linear relations are obtained, as follows:

$$\begin{bmatrix} M_1 & 0 & -u_1M_1 \\ 0 & M_1 & -v_1M_1 \\ \vdots & \vdots & \vdots \\ M_N & 0 & -u_NM_N \\ 0 & M_N & -v_NM_N \end{bmatrix}\begin{bmatrix} p_1 \\ \vdots \\ p_{12} \end{bmatrix}=0 \tag{7}$$

The parameters $(p_1, p_2\ldots\ p_{12})$ are obtained using the direct linear transformation method, while the external parameter matrices R and T of the camera are obtained by decomposition. Specifically, 196 sets of coordinates $(u_i,\ v_i)$ are used to iterate obtain optimal external parameter matrices R and T in each target image. The objective function of obtaining external parameter matrices R and T is to minimize the reprojection error in the iteration process. Therefore, even if image noise, reflection, and uneven illumination cannot accurately detect the pixel coordinates of a single corner, the accuracy of the overall posture can also be guaranteed.

The pose relationship between the CCS and the TCS is obtained as follows:

$$\begin{bmatrix} X_c \\ Y_c \\ Z_c \\ 1 \end{bmatrix} = \begin{bmatrix} R & T \\ 0^T & 1 \end{bmatrix} \begin{bmatrix} X_b \\ Y_b \\ Z_b \\ 1 \end{bmatrix} \tag{8}$$

3.3 Verification of target pose measurement accuracy

In the case of the five-axis motion platform, used in this paper, the respective X, Y, and Z axes are moved in turn, while the corresponding motor encoder values and target image are collected at each axis movement. The actual traveled distance of motor axis, as calculated by the encoder measurements, is considered the actual distance d_a of camera optical center moving in space. The pose matrices R and T of the target, solved by processing the target image, provide the spatial distance variation value, used as the measurement distance d_m of camera optical center moving in space. The deviation d_e between d_a and d_m is calculated, to evaluate the accuracy of target pose measurement by monocular camera.

The experiment considers three groups. In each group of experiments, only one of translational axes of five-axis motion platform was moved, 1 mm each time, and the images were collected at the time of stopping, while it moved continuously for 10 times in one direction. The distance error value d_e, generated at the 10 points in each group motion, is calculated. The experimental results are shown in Fig. 6, where it is illustrated that the distance error caused by moving X and Y axes by single axis can remain below 5 μm. The distance between the camera and the target, in the z-axis direction, will affect the clarity of the recorded image, in the monocular camera measurement system, which will have a greater impact on the results of the target pose measurement. In Fig. 6, the initial moving position of z-axis shows the best focusing results in height. The focus height will gradually change, after continuously moving z-axis, thus affecting the clarity of the image, resulting in an upward trend of the distance error.

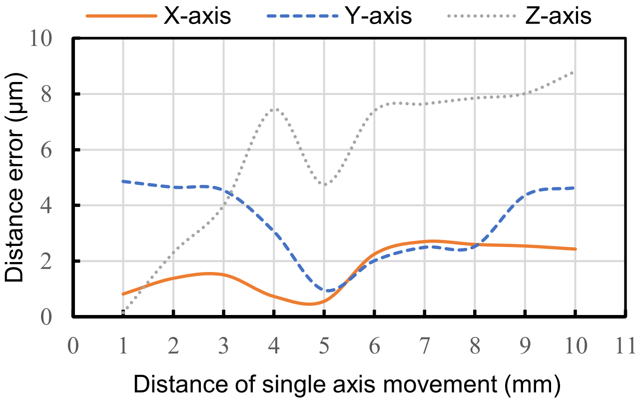

Fig. 6 Verification experiment of monocular vision measurement accuracy

In practice, the camera will be adjusted to the best focus position, in the z-axis direction, so as to collect image data, while the measurement distance error of the camera is limited within a small error range, during the Z-axis motion. Comprehensive analysis shows that the target pose measurement error in this scheme can remain below 10 μm, when the distance between the camera and the target, in the z-axis direction, is well controlled to continuously provide clear recorded image with high measurement accuracy capability. The vision measurement system can meet the pose accuracy requirements, during the calibration process of the five-axis motion platform.

3.4 Comparison of pose estimation with different noise levels

Gaussian noise is added to the target image, and the mean value of Gaussian noise is 0 and the variance is σ. Then the corner detection algorithm used in this paper is compared with that in OpenCV. As shown in Fig. 7, when the value of σ is greater than 0.0003, the corner detection algorithm will detect the corner position by mistake in the target image. However, when the value of σ is greater than 0.0015, the corner position will be detected by mistake in the target image using the detection method in this paper. Let σ change from 0 to 0.0015 for experiment using the pose estimation method in this paper, and get the curve of the reprojection error of target image and the change of σ, as shown in Fig. 8. The experimental results show that the proposed method can accurately measure target pose, even in conditions of image shadow and noise, demonstrating certain robustness.

4 Calibration method for kinematic geometric parameters of five-axis motion platform

Before calibration, the relationship between the motor value $Q_d = [\theta_x, \theta_y, \theta_z, \theta_a, \theta_c]$ of each axis of the five-axis motion platform and the theoretical pose S_d of the TCS, relative to the CCS, can be expressed by the forward kinematics solution

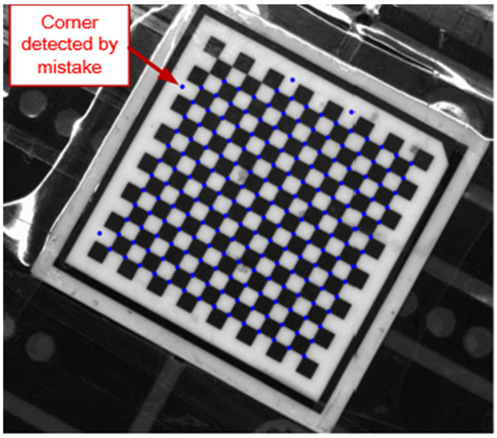

Fig. 7 Display of corner detected by mistake

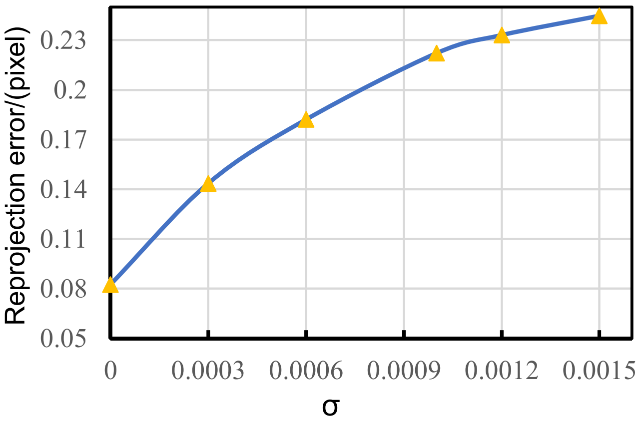

Fig. 8 The curve of the reprojection error of target image and the change of σ

F() and the inverse solution I() of the five-axis motion platform. The θ_x, θ_y, θ_z, θ_a, and θ_c in Q_d represent the position data provided by the motor encoder of X, Y, Z, A, and C axis, respectively:

$$S_d = F(Q_d, \Phi_d) \tag{9}$$

$$Q_\mathrm{d} = I(S_d, \Phi_d) \tag{10}$$

where Φ_d is the nominal value of geometric structure parameters of five-axis motion platform. Due to the PIGEs of the five-axis motion platform, when this is required to move to the specified relative pose S_d, the actual relative pose S_a is as follows:

$$S_a = F(Q_d, \Phi) \tag{11}$$

where $\Phi=\Phi_\mathrm{d}+\Delta\Phi$ is the actual value of geometric structure parameters and $\Delta\Phi$ is the error value of geometric structure parameters. Only when the accurate $\Delta\Phi$ is identified, as far as possible, the accurate forward and inverse solution can be obtained and the final calibration can be realized. The schematic diagram of calibration process is shown in Fig. 9.

An important element of the calibration process is to automatically collect the required data. N images of target were recorded clearly in multiple positions, during the five-axis cooperative motion. According to Eq. (9), the coordinates expression of the TCS origin, relative to the CCS, is obtained, as follows:

$$\begin{cases} x = f_1\left(\theta_x, \theta_y, \theta_z, \theta_a, \theta_c\right) \\ \mathrm{y} = f_2\left(\theta_x, \theta_y, \theta_z, \theta_a, \theta_c\right) \\ z = f_3\left(\theta_x, \theta_y, \theta_z, \theta_a, \theta_c\right) \end{cases} \tag{12}$$

The relationship between x, y, and z and θ_x, θ_y, and θ_z can be expressed linearly, after assigning values to θ_a and θ_c, as:

$$\begin{bmatrix} x \\ y \\ z \end{bmatrix} = M \begin{bmatrix} \theta_x \\ \theta_y \\ \theta_z \end{bmatrix} + \begin{bmatrix} u_1 \\ u_2 \\ u_3 \end{bmatrix} \tag{13}$$

The coefficient matrix M represents the conversion factor, while u_1, u_2, and u_3 represent the constant influence factors on x, y, and z, after the assignment of θ_a and θ_c. The relationship between θ_x, θ_y, and θ_z and x, y, and z can be obtained by matrix transformation, as follows:

$$\begin{bmatrix} \theta_x \\ \theta_y \\ \theta_z \end{bmatrix} = M^{-1} \begin{bmatrix} x-u_1 \\ y-u_2 \\ z-u_3 \end{bmatrix} \tag{14}$$

Let the coordinates of the TCS origin, relative to the CCS, be x_0, y_0, and z_0, when the position of the collected image is the optimal. Based on this condition, n theoretical poses S_{di} are planned. According to Eq. (14), keeping the coordinates of x, y, and z as x_0, y_0, and z_0, the values of θ_x, θ_y, and θ_z, under different values of θ_a and θ_c, are derived, so as to obtain the motor data Q_{di} of N groups of collected images. In addition, the path planning of the motion is conducted so as to avoid collision between the Z-axis and the C-axis of the five-axis motion platform. The motion command is sent by the controller to drive the motor to move to the motor position Q_{di}. Next, the image is collected by the monocular camera, while the target pose is obtained according to the method, presented in Section 2; that is, n actual poses S_{ai} are obtained. Following, the pose error of the five-axis motion platform is determined as follows:

$$\Delta S_i = S_{ai}-S_{di} \tag{15}$$

When the error $\Delta\Phi$ of geometric parameters is small enough, Eq. (15) can be linearized as follows:

$$\Delta S_i = J_i \Delta\Phi \tag{16}$$

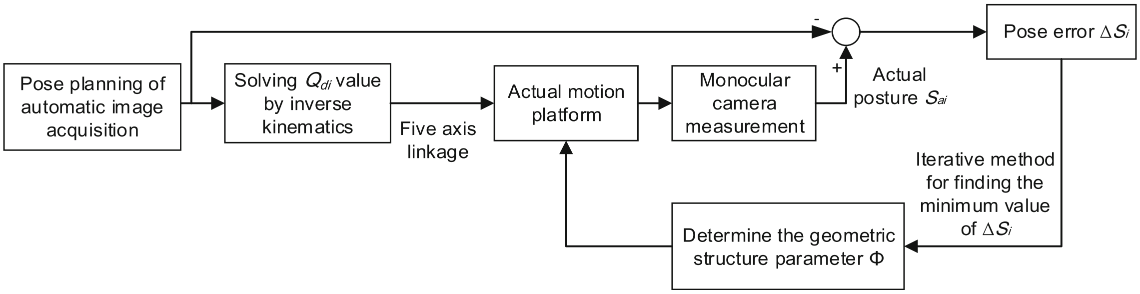

Fig. 9 Schematic diagram of calibration process of five-axis motion platform

$$J_i = \frac{\partial F}{\partial \Phi} \tag{17}$$

where J_i is the Jacobian matrix calculated when the platform is in the i-th pose. Combining Eqs. (16) and (17) results in the following expression:

$$E = J\Delta\Phi \tag{18}$$

where $J = [J_1 \cdots J_i \cdots J_n]^T$ and $E = [\Delta S_1 \cdots \Delta S_i \cdots \Delta S_n]^T$. The optimum value of $\Delta\Phi$, as obtained by the least square method, is as follows:

$$\Delta\Phi = \left[J^T J\right]^{-1} J^T E \tag{19}$$

Equation (19) provides the first estimation of the error value $\Delta\Phi$ of the five-axis motion platform. The value of $\Delta\Phi$ is added to the nominal geometric structure parameters Φ_d, to obtain a new set of geometric structure parameters Φ_j.

This set of Φ_j values, instead of the nominal value Φ_d, is calculated again, within an iterative process, where the geometric structure parameters of the five-axis motion platform can be described as:

$$\begin{cases} \Phi_0 = \Phi_d \\ \Phi_{j+1} = \Phi_j + \Delta\Phi \end{cases} \tag{20}$$

The iteration process continues until ΔS is as small as the termination condition requires, resulting in an accurate geometric structure parameters Φ of the five-axis motion platform.

5 Test experiment of calibration accuracy

After the accurate geometric structure parameters Φ of the five-axis motion platform is identified, the motor axis is moved so that the target image in the camera is clearly at the center of the camera field of view, while the motor value Q_d of the five-axis motion platform is at this time recorded. Substituting the value of Q_d into Eq. (11), the pose matrix of the TCS, relative to the CCS, is obtained. This pose is considered the starting point to rotate around the Z axis of the CCS, in planning a five-axis linkage theoretical pose trajectory T1 of the TCS, relative to the CCS, where the TCS origin is a space circle in the CCS. Through the inverse solution of the kinematics model, the five-axis motor value $Q_{i(0<i<=200)}$ of the five-axis motion platform, corresponding to the theoretical circle trajectory T1, is obtained. The trajectory T1 is shown in Fig. 10.

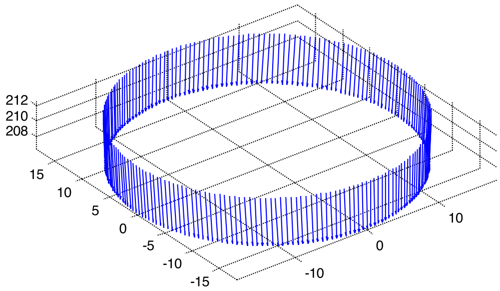

Fig. 10 The trajectory T1

The main computer sends the motor value Q_i to the motion control card to move the five-axis motion platform along the set trajectory T1, executing five-axis cooperative motion. When the five-axis motor value moves to position of Q_i, the camera is used to collect the target image and a total number of 200 images is collected. These images are processed based on the method in Section 2 and the actual pose matrix (R_{ai}, T_{ai}) of the five-axis motion platform is calculated. According to Eq. (11), the theoretical pose matrix (R_{di}, T_{di}), corresponding to the coordinates set Q_i, is calculated. In order to quantify the calibration results, the formulas for solving the position error ΔT_i and orientation error ΔR_i between the actual pose and the theoretical pose are defined as:

$$\Delta T_i = \| T_{ai} - T_{di} \| \tag{21}$$

$$\Delta R_i = \left\| \log\left(R_{ai}^{-1} R_{di}\right)^{\vee} \right\| \tag{22}$$

where v represents the transformation from Lie group to Lie algebra.

In the nominal geometric structure parameters Φ_d of five-axis motion platform, the position error ΔT_i and the orientation error ΔR_i, between the actual and theoretical positions, are calculated by the same method. The accuracy variations by the five-axis motion platform calibration are evaluated according to the differences in position error ΔT_i and orientation error ΔR_i, before and after model calibration. The experimental setup is shown in Fig. 11. The program running on the upper computer is used to collect data, to analyze the calibration results.

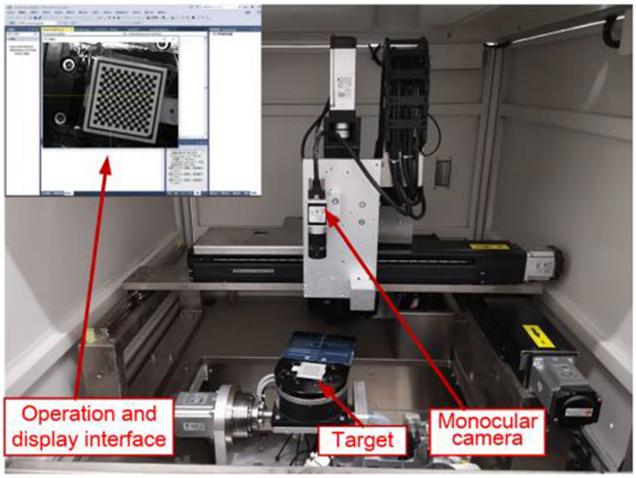

Fig. 11 Experimental equipment

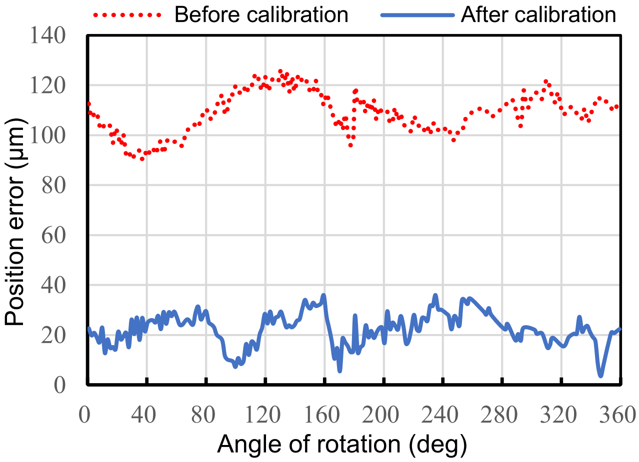

Fig. 12 Comparison of position error before and after calibration of five-axis motion platform

Figure 12 illustrates the position error of the five-axis motion platform, before and after calibration. Before calibration, the average value of the position error of the five-axis motion platform is 108.70 μm, while the maximum value is 125.30 μm. After calibration, the average value of the position error of the five-axis motion platform is reduced to 22.33 μm and the maximum value is reduced to 36.01 μm. Figure 13 shows the direction error, before and after calibration of the five-axis motion platform. Before calibration, the average value of the orientation error of the five-axis motion platform is 0.265° and the maximum value is 0.365°. After the calibration, the average value of the orientation error of the five-axis motion platform is reduced to 0.0357°, and the maximum value is reduced to 0.0789°.

By comparing the experimental data of position and direction errors, before and after calibration, one concludes that the position error and orientation error of the five-axis motion platform are considerably reduced, as a result of the calibration method presented in this paper. The comparison shows that more accurate geometric structure parameters can be obtained after the calibration of the five-axis motion platform, which results in the actual motion trajectory better approximating the theoretical motion trajectory. Furthermore, calibration significantly improves the comprehensive accuracy of the five-axis motion platform

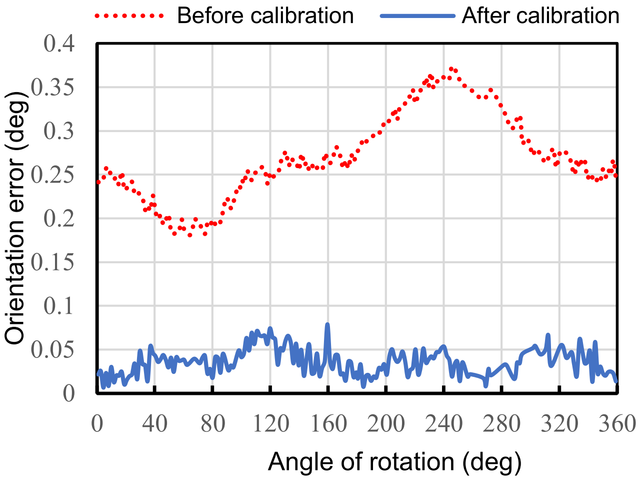

Fig. 13 Comparison of orientation error before and after calibration of five-axis motion platform

6 Conclusions

In order to solve the problems of high measurement cost and complex operation of calibration of five-axis motion platform, this paper presents a designs of simple low-cost operation method, based on monocular vision pose measurement.

(1) The pose measurement method, based on monocular vision, shows high accuracy, as the error of target position measurement remains below 10 μm, even in conditions with image shadow and noise.

(2) The visual pose measurement method is combined with the kinematic loop method, to implement the kinematic model calibration of the five-axis motion platform. The geometric structure parameters of the error model are obtained by the method of equation iteration, while PIGEs are calibrated. After calibration, the average position error of the five-axis motion platform is reduced by 22.33 μm, from 108.70 μm and decreased by 79.46%, while the average value of orientation error is reduced from 0.265 to 0.0357° and decreased by 86.53%. The accuracy of the five-axis motion platform shows significant improvement, which verifies the applicability and effectiveness of the calibration scheme.

Availability of data and material The datasets used or analyzed during the current study are available from the corresponding author on reasonable request.

Code availability Not applicable

Author contribution Not applicable

Funding This work was supported in part by the National Key R&D Program of China (grant number 2017YFB1104800) and the National Natural Science Foundation of China (grant number 51975590).

Declarations

Competing interests The authors declare no competing interests.

References

1. Ekinci TO, Mayer JRR, Cloutier GM (2009) Investigation of accuracy of aerostatic guideways. Int J Mach Tools Manuf 49:478–487. https://doi.org/10.1016/j.ijmachtools.2009.01.001

2. Bringmann B, Knapp W (2006) Model-based 'chase-the-ball' calibration of a 5-axes machining center. CIRP Ann Manuf Technol 55(1):531–534. https://doi.org/10.1016/S0007-8506(07)60475-2
3. Yang H, Huang XD, Ding S, Yu CJ, Yang YM (2018) Identification and compensation of 11 position-independent geometric errors on five-axis machine tools with a tilting head. Int J Adv Manuf Technol 94:533–544. https://doi.org/10.1007/s00170-017-0826-8
4. Alessandro V, Gianni C, Antonio S (2015) Axis geometrical errors analysis through a performance test to evaluate kinematic error in a five axis tilting-rotary table machine tool. Precis Eng 39:224–233. https://doi.org/10.1016/j.precisioneng.2014.09.007
5. Xiang ST, Deng M, Li HM, Du ZC, Yang JG (2019) Volumetric error compensation model for five-axis machine tools considering effects of rotation tool center point. Int J Adv Manuf Technol 102:4371–4382. https://doi.org/10.1007/s00170-019-03497-5
6. Li J, Mei B, Shuai CL, Liu XJ, Liu DW (2019) A volumetric positioning error compensation method for five-axis machine tools. Int J Adv Manuf Technol 103:3979–3989. https://doi.org/10.1007/s00170-019-03745-8
7. Schwenke H, Knapp W, Haitjema H, Weckenmann A, Schmitt R, Delbressine F (2008) Geometric error measurement and compensation of machines—an update. CIRP Ann Manuf Technol 57(2):660–675. https://doi.org/10.1016/j.cirp.2008.09.008
8. Ibaraki S, Knapp W (2013) Indirect measurement of volumetric accuracy for three-axis and five-axis machine tools: a review. Int J Autom Technol 6(2):110–124. https://doi.org/10.3929/ethz-a-007593181
9. Abbaszadeh-Mir Y, Mayer JRR, Cloutier G, Fortin C (2002) Theory and simulation for the identification of the link geometric errors for a five-axis machine tool using a telescoping magnetic ball-bar. Int J Prod Res 40(18):4781–4797. https://doi.org/10.1080/00207540210164459
10. Fan JW, Zhang YL (2020) A novel methodology for predicting and identifying geometric errors of rotary axis in five-axis machine tools. Int J Adv Manuf Technol 108:705–719. https://doi.org/10.1007/s00170-020-05331-9
11. Jiang XG, Cripps RJ (2016) Geometric characterisation and simulation of position independent geometric errors of five-axis machine tools using a double ball bar. Int J Adv Manuf Technol 83(9-12):1905–1915. https://doi.org/10.1007/s00170-015-7711-0
12. Zhang Y, Yang JG, Zhang K (2013) Geometric error measurement and compensation for the rotary table of five-axis machine tool with double ballbar. Int J Adv Manuf Technol 65(1-4):275–281. https://doi.org/10.1007/s00170-012-4166-4
13. Ibaraki S, Oyama C, Otsubo H (2011) Construction of an error map of rotary axes on a five-axis machining center by static R-test. Int J Mach Tool Manu 51:190–200. https://doi.org/10.1016/j.ijmachtools.2010.11.011
14. Hong C, Ibaraki S, Oyama C (2012) Graphical presentation of error motions of rotary axes on a five-axis machine tool by static R-test with separating the influence of squareness errors of linear axes. Int J Mach Tools Manuf 59:24–33. https://doi.org/10.1016/j.ijmachtools.2012.03.004
15. Chen YT, More P, Liu CS, Cheng CC (2019) Identification and compensation of position-dependent geometric errors of rotary axes on five-axis machine tools by using a touch-trigger probe and three spheres. Int J Adv Manuf Technol 102:3077–3089. https://doi.org/10.1007/s00170-019-03413-x
16. Chen YT, More P, Liu CS (2019) Identification and verification of location errors of rotary axes on five-axis machine tools by using a touch-trigger probe and a sphere. Int J Adv Manuf Technol 100:2653–2667. https://doi.org/10.1007/s00170-018-2863-3
17. Mchichi NA, Mayer JRR (2019) Optimal calibration strategy for a five-axis machine tool accuracy improvement using the D-optimal approach. Int J Adv Manuf Technol 103:251–265. https://doi.org/10.1007/s00170-019-03454-2
18. IBARAKI S, TANIZAWA Y (2011)Vision-based measurement of two-dimensional positioning errors of machine tools. J Adv Mechan Design Syst Manuf 5(4):315–328. https://doi.org/10.1299/jamdsm.5.315
19. Liu W, Li X, Jia ZY, Li H, Ma X, Yan HY, Ma JW (2017) Binocular-vision-based error detection system and identification method for PIGEs of rotary axis in five-axis machine tool. Precis Eng 51:208–222. https://doi.org/10.1016/j.precisioneng.2017.08.013
20. Li X, Liu W, Pan Y, Ma JW, Wang FJ (2019) A knowledge-driven approach for 3D high temporal-spatial measurement of an arbitrary contouring error of CNC machine tools using monocular vision. Sensors 19(3):744. https://doi.org/10.3390/s19030744
21. Wang D, Bai Y, Zhao J (2012) Robot manipulator calibration using neural network and a camera-based measurement system. Trans Inst Meas Control 32(1):105–121. https://doi.org/10.1177/0142331210377350
22. Stepanova K, Pajdla T, Hoffmann M (2019) Robot self-calibration using multiple kinematic chains—a simulation study on the iCub humanoid robot. IEEE Robot Auto Lett 4:1900–1907. https://doi.org/10.1109/LRA.2019.2898320
23. Wang H, Lu X, Hu Z, Li Y (2015) A vision-based fully-automatic calibration method for hand-eye serial robot. Ind Robot 42(1):64–73. https://doi.org/10.1108/IR-06-2014-0352
24. Urban S, Leitloff J, Hinz S (2015) Improved wide-angle, fisheye and omnidirectional camera calibration. ISPRS J Photogramm Remote Sens 108:72–79. https://doi.org/10.1016/j.isprsjprs.2015.06.005
25. Zhu HJ, Li Y, Liu X, Yin XH, Shao YH, Qian Y, Tan JD (2020) Camera calibration from very few images based on soft constraint optimization. J Franklin Instit 357(4):2561–2584. https://doi.org/10.1016/j.jfranklin.2020.02.006
26. Zhang ZY (1999) Flexible camera calibration by viewing a plane from unknown orientations. Proc Seventh IEEE Int Confer Comput Vis 1:666–673. https://doi.org/10.1109/ICCV.1999.791289
27. Geiger A, Moosmann F, Car O, Schuster B (2012) Automatic camera and range sensor calibration using a single shot. IEEE Int Confer Robot Auto 2012:3936–3943. https://doi.org/10.1109/ICRA.2012.6224570
28. Zhu Q, Wu B, Wan N (2007) A sub-pixel location method for interest points by means of the Harris interest strength. Photogramm Rec 22:321–335. https://doi.org/10.1111/j.1477-9730.2007.00450